Simplified Reeb Graph as Effective
Shape Descriptor for the Striatum

Pepe A.[1]*, Brandolini L.[2]*, Piastra M.[2], Koikkalainen J.[3], Hietala J.[4], and Tohka J.[1]
* These two authors contributed equally to the work.

[1] Tampere University of Technology, P.O. Box 553, 33101, Tampere, Finland
[2] Universitá di Pavia, via Ferrata 1, Pavia, Italy
[3] VTT Technical Research Centre of Finland, P.O. Box 1300, FIN-33101 Tampere, Finland
[4] University of Turku, FIN-20700 Turku, Finland and Turku PET Centre, Finland

Abstract. In this work, we present a novel image and mesh processing pipeline for the computation of simplified Reeb graphs for closed triangle meshes of the human striatum extracted from 3D-T1 weighted MR images. The method uses active contours for computing the mesh partition and the simplified Reeb graph. Experimental results showed that simplified Reeb graphs, as obtained by our pipeline, provide an intrinsic, effective, and stable descriptor of striatal shapes to be used as an automatic tool for inter-subject mesh registration, mesh decomposition, and striatal shapes comparison. Particularly, the nodes of simplified Reeb graphs proved to be robust landmarks to guide the mesh registration. The quality of the inter-subject mesh registration obtained by the use of simplified Reeb graphs slightly outperformed the one obtained by surface-based registration techniques. In addition, we show the stability of the resulting mesh decomposition, and we propose its use as an automatic alternative to the manual sub-segmentation of the striatum. Finally we show some preliminary results on the inter-group comparisons among neuroleptic-naive schizophrenic patients and matched controls.

Keywords: Simplified Reeb Graph, Surface Registration, Mesh Decomposition, Striatum, Schizophrenia, MRI

1 Introduction

Human striatum is an highly innervated group of nuclei in the brain, and the primary receiver of afferent nerves from the cerebral cortex and thalamus to the basal ganglia [1]. Striatum is implicated, via the cortico-striato-thalamo-cortical circuitry, in motor processes, such as spatial orientation and movement selection, and in a number of non-motor processes such as cognitive functions, learning, attention, memory, motivation, reward, and addiction [2–4]. Striatum can be anatomically divided into three primary regions: caudate, putamen, and nucleus accumbens. Different striatal regions are thought to receive projections from different cortical regions [5]. Particularly, caudate appears to have greater connectivity to prefrontal regions, and thus to be more critical in cognitive and memory functions than putamen [2]. Putamen appears to have connectivity with more posterior cortical regions than the caudate, and thus to be crucial to motor processing, and to subserve cognitive functions more limited to stimulus-response [2, 3]. Striatal structures, due to their cognitive and motor functions, are of high interest in

schizophrenia. In this disease, cognitive functions are impaired. Furthermore, parkin-sonian and extrapyramidal (dyskinesias) signs have been reported in neuroleptic-naïve patients presenting schizophrenia [6]. The nucleus accumbens is a central part of limbic and prefrontal cortico-striato-pallidal-thalamic circuits, and it is involved in cognitive, emotional and psychomotor functions, which are often disturbed in schizophrenia [1].

In addition to volumetric studies [7, 1], local and global morphometric approaches have been proposed for the analysis of the striatal shape and its aberrations in health and schizophrenia. Among the local shape approaches, [8] used the deformation fields required to warp an individual image to a reference template image as a basis for the analysis of localized shape changes; while [4] presented methods for the analysis of detailed 3D surface models after their macroscopic differences were removed (surface registration or matching). Deformation and surface based methods provide spatially localized shape information that is relatively straightforward to interpret; however, they usually require the establishment of the point correspondence among surfaces [9]. Except if ad-hoc strategies are used [10], the establishment of the point correspondence is computationally demanding, and it often requires remeshing.

Global shape approaches have been used in medical imaging for the compact representation and analysis of neuroanatomical shapes. Particularly, [11] used medial representation to study shape differences in schizophrenia; [12] used spherical harmonic description to study the shape changes in striatum with bipolar disorder; [9] used Laplace-Beltrami eigenvalues for shape comparisons of hippocampus based on selected eigenfunctions. Furthermore, [13] proposed an algorithm for mesh partitioning and skeletonization using a shape diameter function.

In this paper we propose the adoption of Reeb graphs as compact descriptors for the striatal shape. Indeed, Reeb graphs are more robust than other skeletal descriptors since they are less sensitive to small and localized changes on the mesh [14].

The definition of a Reeb graph [15] for a closed and connected surface is based on the concept of Morse function [16, 17], which is a scalar function defined on the surface, having only *maxima*, *minima* and *saddles* as critical points. In particular a Morse function does not have *degenerate saddles* (see definitions in [18]). The Reeb graph is related to the level lines of the Morse function on the surface; each point in the Reeb graph corresponds to a connected component of a level line of the Morse function. More precisely, the nodes in the Reeb graphs correspond to the connected component containing critical points and the arcs correspond to sets of connected components containing only regular (i.e. non-critical) points of the Morse function. As a remarkable property, the number of loops of the Reeb graph of a closed, connected surface is equal to the *genus* of the surface [19]. In practical applications, Reeb graphs are complemented by a geometric embedding by which each point in the Reeb graph is positioned at the centroid of the corresponding connected component. In addition, the extraction of the Reeb graph is often seen as part of a *mesh decomposition* (also referred as *mesh partitioning* or *surface segmentation* procedure), in which the connected components containing critical points of the Morse function serve as the boundaries of different surface *segments*.

The discrete variants of Reeb graphs have been broadly applied in recent years in different fields of computer vision with the role of compact shape descriptors [18], starting from the seminal works [20, 21]. In [22], an interesting definition is given in terms of

level-set diagrams, for 0-genus surfaces. [30] uses a geodesic function defined on the surface for object recognition. The concept in [22] is further expanded in [23], where the definition of a Morse function intrinsic to the surface was proposed, although with a random choice of the starting vertex as seed. The latter method uses evolving contours that also compute the mesh partitioning into segments, but the method may incur in critical contour configurations, especially in the case of coarser meshes. [24] proposed an on-line algorithm for Reeb graphs construction that takes into account all the simplicial elements of the mesh; the algorithm was validated with several different Morse functions but it does not compute a mesh partitioning. [25] described an approach based on dynamic graphs that are directly constructed from the critical points of the Morse function; the method however does not extract the level lines and this makes it difficult to compute the geometric embedding. In [26] Reeb graphs were applied to produce mesh decomposition with the use of average geodesic distance calculated from a small set of evenly-spaced vertices (base vertices), but no embedding is proposed for the graphs. [27] proposed an approach based on critical points and their isocontours, which is particularly suited for large meshes with small genus, for which 'smooth' Morse functions can be defined. The algorithm proposed in [28], which is derived from that in [23], uses evolving *active* contours for computing a mesh partitioning into segments, hence a *simplified* version of the Reeb graph in which each node corresponds to the centroid of an entire segment and the arcs describe the adjacency relations between segments.

In this paper, we adopt a variation of [28] to compute the simplified Reeb graph (SRG) for closed triangle meshes extracted from 3D T1-weighted brain MR images of the human striatum. This algorithm is particularly robust with respect to mesh density (number of vertices in the mesh) and to surface genus [28]. The goal of this work, behind the one of proposing the use of SRG as a compact descriptor of the striatal shape, was to explore the effectiveness of such a descriptor for the purpose of automatic inter-subject mesh registration (a), automatic mesh decomposition (b), and for the inter-group striatal shapes comparison (c).

(a) To assess the significance of the SRG-based registration as compared to other surface-based registration techniques (registration performed i.e. by establishing the point correspondence among the surface vertices on the entire mesh), we used a test set collected from neuroleptic-naive patients presenting schizophrenia and matched controls. The quality of the SRG based striatal mesh registration slightly outperformed the one obtained by surface-based registration techniques.

(b) Striatal structures, each of which is implicated in different functions, are differently affected in schizophrenia [7]. Striatal sub-segmentation is challenging as the signal intensity alone is not sufficient to distinguish among its sectors [29], and manual or semi-automatic methods are still regarded as the gold standard. We present here an automatic striatal mesh decomposition into its three primary anatomical regions (caudate, putamen and nucleus accumbens). The sub-segmentation is obtained as a direct result of the SRG extraction and it does not involve any registration to labelled images or any a priori information on the striatal surface. Our results, albeit not quantitatively validated, appeared as a promising, robust and repeatable alternative to the laborious manual methods.

(c) In this work we found that, despite their compactness, SRG are sensible to shape variations of the striatum. This result inspires further investigations on the use of the
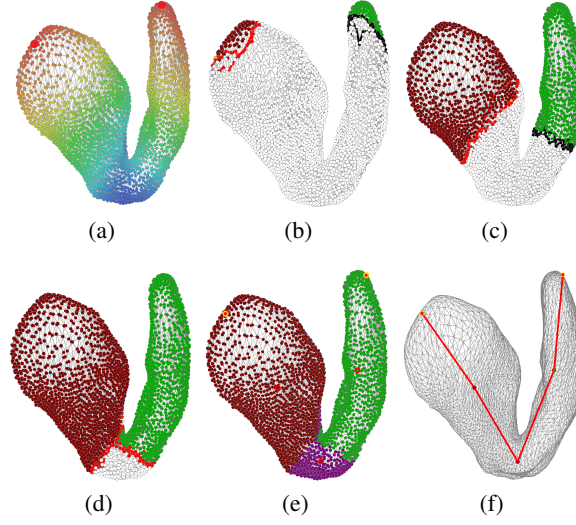
Fig. 1: Vertices colors represent increasing values (from dark red to dark blue) of the Morse function; feature points are magnified and represented in red. (a). Active contours start at each feature point (b) and they are evolved in the direction of ascending values of the Morse function (c). Two active contours merge in a new one (d). Each node in the SRG is either a feature point or the centroid of a segment (e), arcs of the SRG describe adjacency relations (f).

SRG descriptor for the detection and analysis of neuroanatomical morphological differences within and between groups.

2   Methods

2.1   Computing the Simplified Reeb Graph

Computing the Morse Function   A critical aspect in extracting the Reeb graphs from surfaces is the choice of a proper Morse function [31, 23]. The Morse function we adopted is based on the concept of *geodesic distance* on a mesh [32, 33], i.e. the length of the shortest path connecting each two vertices. We first find the two *diameter vertices*, which are the pair of vertices at maximum geodesic distance. We then compute two distance functions, one for each of the diameter vertices, and we determine the *local maxima* and *minima* of each distance function (*local extrema*). The local extrema are then merged, with some tolerance: pairs of local extrema from each of the two functions are merged into a common *feature point* if they are not farther away than a certain predefined tolerance, otherwise they are simply discarded. By definition, the value of the Morse function of choice at each vertex is the geodesic distance to the closest feature point (see fig. 1(a)). The main advantage of this Morse function, which is a variant of those proposed in [23] and [22], is that the feature points correspond to prominent points of the shape and the resulting Morse function is intrinsic to the surface, in that it is independent from rotation and scaling.

Segmentation and Construction of the SRG   An *active contour* is a discrete, connected, closed line, made of vertices and edges, that represents the advancing front

between the vertices that have been visited and the rest of the mesh. Active contours are initialized at each feature point (see fig. 1(b)), i.e. a minimum of the Morse function of choice. Active contours are then evolved in the direction of ascending values of the Morse function in a synchronized fashion (see fig. 1(c)); at each step, the vertex having the lowest value in all active contours is selected as the *candidate vertex* and the corresponding active contour is evolved. If the candidate is not a critical vertex, the selected active contour is just advanced locally, in the neighborhood of the vertex itself. The update is more complex if the candidate is a critical vertex, in particular a saddle. In fact, two types of event can occur at a saddle vertex:

- a *split* - the active contour is self-intersecting and is therefore split into two new active contours;
- a *merge* - the active contour came in touch with another one and the two are merged into a new active contour.

The update is straightforward when the candidate vertex is a maximum, as the selected active contour simply vanishes. The algorithm terminates when all active contours have vanished. The partition of the mesh into *segments* is constructed incrementally during the evolution of active contours. Away from critical vertices, all newly visited vertices are added to the corresponding segment. When either a split or a merge event occurs, all segments are closed and new segments are created. More precisely, when a split event occurs the splitting segment is closed and two new segments are created, whereas when a merge event occurs, the two merging segments are closed and a new segment is created (see fig. 1(d)). The overall mesh partitioning is described by the collection of all segments thus obtained. The simplified Reeb graph contains a node corresponding to the centroid of each of the segments (see fig. 1(e)) and the arcs represent the adjacency relations between the segments. The graph is completed by the nodes representing the feature points, together with an arc between each of them and the centroid of the segment in which they are contained (see fig. 1(f)).

The algorithm also contains special provisions for dealing with irregular cases, not described above, that occur more frequently with coarse meshes and/or with higher genus. See [28] for details.

2.2 Striatum shape processing

Material In this study, we used 3-D T1-weighted MR brain images of 40 subjects (22 normal controls, and 18 neuroleptic-naïve patients presenting first-episode schizophrenia or schizoaffective disorder) previously described in [34]. This study was performed in accordance with the Declaration of Helsinki. The ethic committee of the Turku Central Hospital supervised and approved the experimental procedure. A written informed consent was collected from all of the participants enrolled in the study. MRI brain scans were acquired using a 1.5 T Siemens Magnetom (Erlangen, Germany) as detailed in [34]. The voxel size of the MR images was $1.5 \times 1.5 \times 1.0$ mm^3 and the size of the images varied from $256 \times 256 \times 150$ to $256 \times 256 \times 170$ voxels.

MRI to Mesh MR images were manually segmented using a 3D software tool for interactive construction of individualized surface models with topologically correct triangulation [35, 4]. With this 3D tool, the striatum (not including the tail of the caudate) was manually segmented in each MRI volume by non-rigid deformation of a same triangulated surface model to the edges of the striatum. The obtained striatal surfaces were decomposed into two mesh surfaces representing the left and right striatum separately.
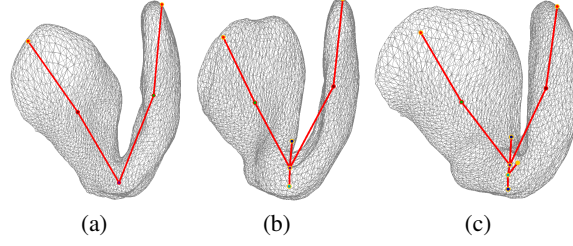
(a)   (b)   (c)

Fig. 2: SRG obtained by applying the proposed algorithm to three examples of striatal shapes.

Computing SRG The SRG-algorithm (Section 2.1) was applied to each mesh to obtain a simplified Reeb graph and a mesh partitioning. A typical aspect of discrete Morse functions is that, depending on both the shape and the triangulation, they may have several extra maxima which generate extra branches in the Reeb graph (see Fig. 2). Nevertheless, given that all the striatum meshes have genus 0, the extracted Reeb graphs are guaranteed to contain no loops. In this specific case, this means that all extra branches had a common root and that the corresponding segments could be safely merged with the root segment. This also entailed recomputing the centroid of the root segment after the extra segments had been merged. As a result of this procedure, all the SRG had the same number of nodes.

2.3 SRG-based Registration of Striatal Meshes

We developed an iterative algorithm for the 7-parameter linear registration of striatal surfaces by matching their SRG descriptors using Full Procrustes Superimposition [36] (FPS). The algorithm is composed of three consecutive steps:

Step 1: One of the N graphs $x_i, i = 1, ..., N$, is randomly selected as a reference x^r. All other graphs x_i are registered to x^r by minimization of the sum of square differences $\sum_{j=1}^{V} \|x_j^r - (s_i \mathbf{R}_i x_{i,j} + \mathbf{t}_i)\|^2$ w.r.t. $s_i, \mathbf{t}_i, \mathbf{R}_i$ using FPS. Here $V = 5$ is the number of nodes in each graph; x_j^r and $x_{i,j}$ are the 3D coordinates of the j-th node of the reference graph and of the i-th individual graph, respectively; $s_i, \mathbf{t}_i, \mathbf{R}_i$ are the isotropic scaling factor, translation vector, and rotation matrix, for the i-th graph respectively.

Step 2: After step 1, each graph is aligned to x^r. To make sure that the quality of the SRG superimposition is not affected by the particular choice for the reference graph[1], a further iterative registration routine is implemented:

(i) Calculate the mean shape of the SRG which were registered to x^r as the arithmetic mean of the registered graphs. If $\tilde{x}_i$ denotes the i-th registered graph, the mean shape is $\tilde{x}_j^m = (1/N) \sum_{i=1}^{N} \tilde{x}_{i,j}, \forall j = 1, ..., V$.
(ii) Pre-registered graphs ($\tilde{x}_i$) are aligned to $\tilde{x}^m$ by minimizing $\sum_{j=1}^{V} \|\tilde{x}_j^m - (\tilde{s}_i \tilde{\mathbf{R}}_i \tilde{x}_{i,j} + \tilde{\mathbf{t}}_i)\|^2$ w.r.t. $\tilde{s}_i, \tilde{\mathbf{t}}_i, \tilde{\mathbf{R}}_i$ using FPS.
(iii) The mean shape of the graphs is updated and the transformation $T(\tilde{s}, \tilde{\mathbf{t}}, \tilde{\mathbf{R}})$ is composed to the one calculated at the previous stages.

Points (ii) and (iii) are repeated until a maximum number of iterations is achieved or until there are no improvements to the SRG superimposition.

---

[1] Particularly, the registration accuracy might be significantly impaired if the reference graph is not a good representative of the mean SRG in the dataset.
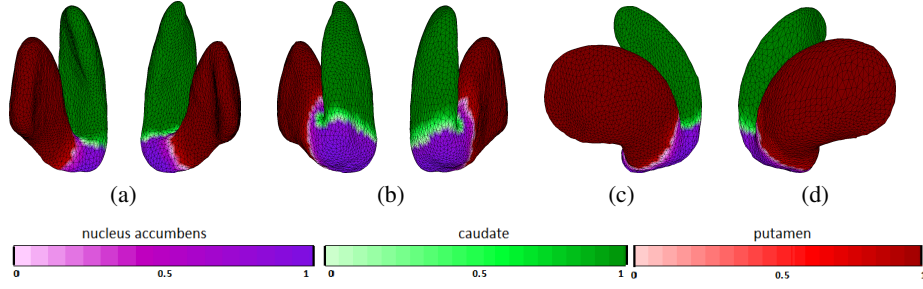
Fig. 3: Probabilistic maps of the left and right striatal mesh decomposition, for the whole database, depicted in frontal (a), posterior (b), and lateral (c and d) views. Maps were obtained by calculating the probability of each surface vertex to be assigned to each mesh sector. Notice how the mesh decomposition of the striatal shapes into three sectors actually corresponds to the anatomical sub-segmentation of human striatum into nucleus accumbens (violet), caudate (green) and putamen (red).

Step 3: The composed transformation $T(\tilde{s}, \tilde{\mathbf{t}}, \tilde{\mathbf{R}})$ that best matches each SRG to the mean graph shape is applied to the corresponding meshes (the ones from which the SRG were extracted from).

3 Results

3.1 Assessment of SRG-based Surface Decomposition

As a result of the automatic SRG extraction and consequent mesh decomposition, three distinct mesh sectors were obtained for each striatal surface. By visual inspection, results of the mesh decomposition were consistent within (left and right striatum) and between subjects, for the whole database. An example of mesh decomposition produced by our pipeline is depicted in Fig. 1.(e).

A probabilistic map of the resulting striatal decomposition was then obtained by calculating the probability of each surface vertex to be assigned to each mesh sector in the whole database. This mesh decomposition into three sectors corresponded to the anatomical sub-segmentation of human striatum into nucleus accumbens, caudate and putamen (depicted in Fig. 3 in violet, green and red colors, respectively).

3.2 Assessment of SRG-based Registration of Striatal Meshes

The SRG-based registration routine described in Section 2.3 was used for the linear alignment of striatal surfaces (left and right striatum separately). For comparison, the same striatal meshes were also linearly aligned to each other with the same method illustrated in Section 2.3 but applied to the whole mesh: the linear transformation is extracted using all the vertices of the mesh, and is then applied to the corresponding SRG. For further comparison, a second surface-based registration routine similar to the one in [4] was also applied: a mean mesh was calculated and all the individual meshes were affinely registered to that using Arun's method [37]; the mean mesh was finally registered back to the previously (affinely) registered meshes using again [37]. Examples of the SRG and striatal meshes, prior and after registration, are shown in Fig. 4.

Table 1: Accuracy of the SRG-based registration compared to the surface-based registration. The accuracy of the striatal mesh registration was evaluated with two measures derived from the Hausdorff distance.

| | SRG-based | | surface-based | | | |
| | FPS^2 | | FPS ^{2} | | Arun | |
	Left	Right	Left	Right	Left	Right
HD_1 [mm]	3.4751	2.9124	3.4187	3.0510	3.4264	3.1653
HD_2 [mm]	4.8307	4.1326	4.8512	4.3999	4.9386	4.6012

Since a ground truth for the striatal surface registration was not available, we quantitatively compared the results of the SRG-based registration of striatal meshes to the aforementioned (using FPS and Arun's method) more traditional surface-based methods. Results were quantitatively validated using the Hausdorff Distance (HD) (see Table 1). The HD [38] provides a measure of the maximum symmetrical distance between two surfaces and thus can be used to validate the surface registration. Particularly, two measures based on the HD (denoted as d) were computed:

– HD_1: mean of the HD computed between each registered surface and the mean surface mesh, $\frac{1}{N} \sum_{i=1}^{N} d(\tilde{x}_i, \tilde{x}^m)$. HD_1 can be interpreted as a measure of the dispersion of the registered surfaces as compared to the mean shape, and therefore as a measure of the remaining mis-alignment.

– HD_2: mean of the HD computed for each mesh with respect to each other mesh $\frac{1}{N(N-1)/2} \sum_{i=1}^{N} \sum_{l=i+1}^{N} d(\tilde{x}_i, \tilde{x}_l)$. HD_2 can be interpreted as a measure of the mean maximal difference between each pair of surfaces in the database (after their alignment), and therefore also as a measure of the shape variability within the given dataset.

The registration accuracy obtained by the use of SRG was qualitatively (see Fig. 4) and quantitatively (as measured by the HD, see Table 1) comparable to, and in some cases outperforming, the registration accuracy obtained by more classical surface-based approaches.

In the surface-based registration algorithms, optimal registration parameters in the presence of point correspondence are estimated using all surface vertices. The establishment of the point correspondence is however computationally demanding, especially for dense surfaces, and it often requires remeshing (which could in turn influence shape comparisons done on surfaces [9]). On the other hand, our experimental results suggest that using a surface representation of the striatal shapes, although its importance for characterizing non-rigid motion remains unquestionable, is overly redundant in case of 7-parameter linear motion if an SRG descriptor of that shape can be extracted. The SRG-based registration proposed here only requires triangulated closed meshes and it is not limited to meshes having a same number of vertices. As a consequence, the implications of these results might be extended to other shapes than the human striatum, although further testing is required.

---

[2] Similar results were obtained if the optimization of the transformation was obtained (the absolute orientation problem) using Horn's quaternion-based closed form solution [39].
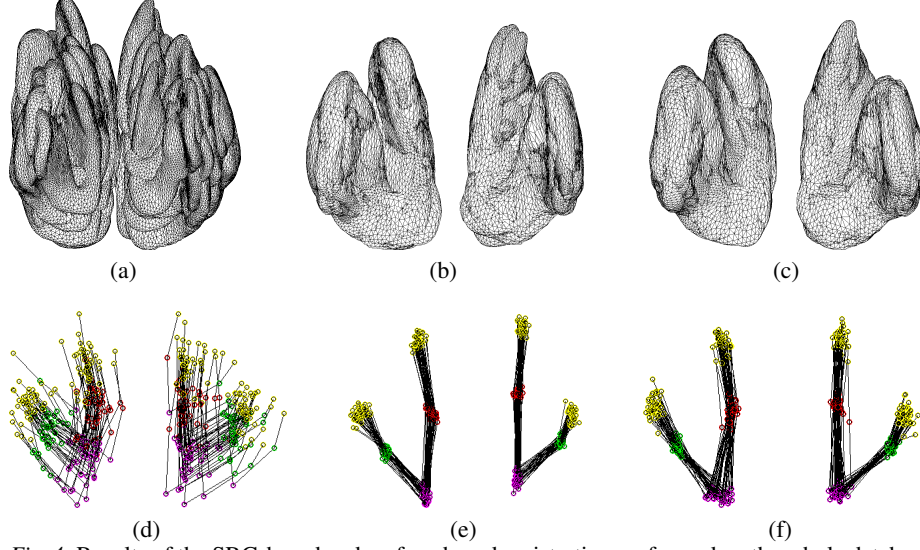
Fig. 4: Results of the SRG-based and surface-based registration performed on the whole database consisting of 40 subjects. In the first column, striatal meshes in the native space (a) are shown with their corresponding SRG (d). In the second column, the SRG in the native space (d) are aligned by SRG-based registration (e) and the obtained transformations are applied to the corresponding meshes (a) to obtain (b). In the third column, meshes in the native space (a) are aligned by a surface-based registration using FPS (c) and the obtained transformations are applied to the corresponding SRG graphs (d) to obtain (f).

3.3   Stability of the SRG to Mesh Resolution

The SRG is stable to different mesh resolutions. Applying the SRG algorithm to meshes progressively decimated we can see that the resulting segmentation is robust and stable, and the corresponding SRG are consistent in that they contain the same number of nodes (see Fig. 5).

3.4   Shape Representation

The robustness of SRG to mesh resolution, besides confirming the legitimacy of using the nodes of the graph as robust landmarks to guide the registration, also motivated their use as descriptors for group-specific mean shapes. Particularly, the analysis of the mean SRG obtained in schizophrenia and control groups (Fig. 6) showed that, despite the compactness of the SRG descriptor, it is sensible to mesh variations. The use of simplified Reeb graphs as a tool for studying the intra-group shape variability (or for discriminating among groups based on their shapes) was out of the scope of this work and has not been explored further. Nevertheless, our results inspires further investigations on the use of the SRG descriptor for the detection and analysis of neuroanatomical morphological differences within and between groups.

4   Conclusions

In this work, we presented an image and mesh processing pipeline that uses SRG as a faithful and effective shape descriptor for the striatal shapes extracted from 3D T1-weighted MR images. To the best of our knowledge, this is the first study proposing this
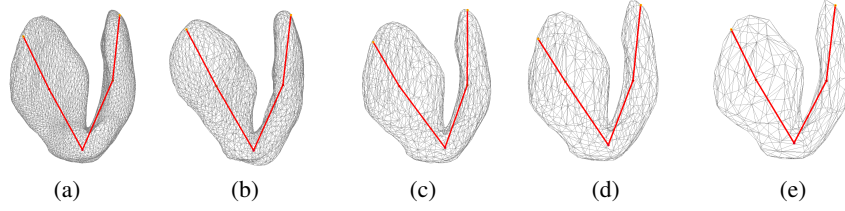
Fig. 5: The SRG is robust to mesh resolution. These are SRG of the same mesh progressively decimated: 3293 vertices (a), 1647 vertices (b), 824 vertices (c), 413 vertices (d), 207 vertices (e).

(a)
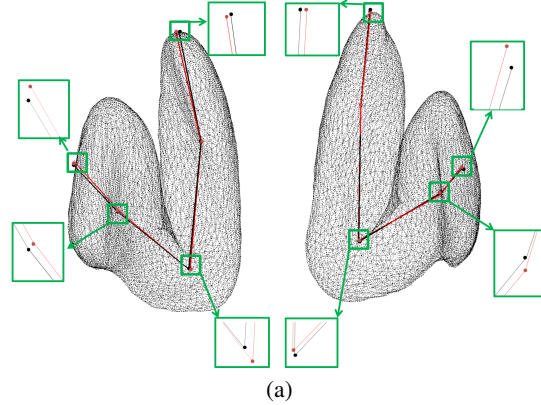
Fig. 6: The figure shows the mean SRG in schizophrenia (depicted in red) and in normal controls (depicted in black) overlaid to the mean striatal surface in frontal view. This is an illustration of the potentialities of the SRG as a descriptor for group-specific mean shapes, although we are aware that the role of this descriptor as a tool to discriminate among groups has not been validated, and no medical conclusions should be derived from it.

kind of shape descriptor for the human striatum. Due to its geometrical and topological properties, SRG is robust to small local variations on the mesh, and as such, effective as a basis for inter-subject registration, shape representation, and mesh decomposition of striatal surfaces.

The results presented showed that the registration obtained with the proposed method is qualitatively comparable and quantitatively (as measured by the Hausdorff distance) outperforming the surface-based registration, while being computationally simpler. Indeed, the SRG-based registration does not require neither the computation of the point correspondence among mesh vertices, nor is limited to meshes having a same number of vertices. The results show also the efficacy of SRG for mesh partitioning: albeit not quantitatively validated, the sub-segmentation of the striatal surfaces into caudate, putamen, and nucleus accumbens are qualitatively meaningful. Finally, the results showed that, despite its compactness, SRG can be used as a compact descriptor for group specific mean-shapes of the human striatum.

References

1. M. Lauer, D. Senitz, and H. Beckmann, "Increased volume of the nucleus accumbens in schizophrenia," *J. Neural Transmission*, vol. 108, pp. 645–660, 2001.

2. A. Brickman, M. Buchsbaum, L. Shihabuddin, E. Hazlett, J. Borod, and R. Mohs, "Striatal size, glucose metabolic rate, and verbal learning in normal aging," *Cognitive Brain Res.*, vol. 17, no. 1, pp. 106 – 116, 2003.

3. J. Grahn, J. Parkinson, and A. Owen, "The cognitive functions of the caudate nucleus," *Prog. Neurobiol.*, vol. 86, no. 3, pp. 141 – 155, 2008.

4. J. Koikkalainen, J. Hirvonen, M. Nyman, J. Lötjönen, J. Hietala, and U. Ruotsalainen, "Shape variability of the human striatum - effects of age and gender," *NeuroImage*, vol. 34, no. 1, pp. 85 – 93, 2007.

5. C. Seger, "How do the basal ganglia contribute to categorization? their roles in generalization, response selection, and learning via feedback," *Neurosci. Biobehav.l R.*, vol. 32, no. 2, pp. 265 – 278, 2008.

6. R. McCreadie, T. Srinivasan, R. Padmavati, and R. Thara, "Extrapyramidal symptoms in unmedicated schizophrenia," *J. Psychiat. Res.*, vol. 39, no. 3, pp. 261 – 266, 2005.

7. M. S. Buchsbaum, L. Shihabuddin, A. Brickman, R. Miozzo, R. Prikryl, R. Shaw, and K. Davis, "Caudate and putamen volumes in good and poor outcome patients with schizophrenia," *Schizophr. Res.*, vol. 64, no. 1, pp. 53 – 62, 2003.

8. H. Volz, C. Gaser, and H. Sauer, "Supporting evidence for the model of cognitive dysmetria in schizophrenia - a structural magnetic resonance imaging study using deformation-based morphometry," *Schizophr. Res.*, vol. 46, no. 1, pp. 45 – 56, 2000.

9. M. Reuter, F. Wolter, M. Shenton, and M. Niethammer, "Laplace - beltrami eigenvalues and topological features of eigenfunctions for statistical shape analysis," *Comput. Aided Design*, vol. 41, no. 10, pp. 739 – 755, 2009.

10. A. Pepe, L. Zhao, J. Tohka, J. Koikkalainen, J. Hietala, and Ruotsalainen, "Automatic statistical shape analysis of local cerebral asymmetry in 3d t1-weighted magnetic resonance images," in *In Proc. of MICCAI 2011 MedMesh workshop*, pp. 127–134, R.R. Paulsen and J.A. Levine.

11. Y. Sampath, K. Vetsa, M. Styner, S. Pizer, J. Lieberman, and G. Gerig, "Caudate shape discrimination in schizophrenia using template-free non-parametric tests.," in *In Proc. of MICCAI 2003*, p. Part II, 2003.

12. J. Hwang, I. Lyoo, S. Dager, S. Friedman, J. Oh, J. Y. Lee, S. Kim, D. Dunner, and P. Renshaw, "Basal ganglia shape alterations in bipolar disorder.," *Am. J. Psychiatry*, vol. 163, no. 2, pp. 276–285, 2006.

13. L. Shapira, A. Shamir, and D. Cohen-Or, "Consistent mesh partitioning and skeletonization using the shape diameter function," *Visual Comput.*, vol. 24, pp. 249–259, 2008.

14. Y. Shi, R. Lai, S. Krishna, I. Dinov, and A. Toga, "Anisotropic laplace-beltrami eigenmaps: Bridging reeb graphs and skeletons.," in *In Proc. of CVPR 2008 Workshop*, (Anchorage, AK, USA), pp. 1–7, IEEE Computer Society, 2008.

15. G. Reeb, "Sur les points singuliers d une forme de pfaff completement integrable ou d une fonction numerique.," in *Comptes rendus de l'Academie des Sciences 222*, pp. 847–849, 1946.

16. J. Milnor, *Morse theory*, vol. 51. Princeton Univ Pr, 1963.

17. T. Banchoff, "Critical points and curvature for embedded polyhedral surfaces," *T. Am. Math. Mon.*, vol. 77, no. 5, pp. 475–485, 1970.

18. S. Biasotti, D. Giorgi, M. Spagnuolo, and B. Falcidieno, "Reeb graphs for shape analysis and applications," *Theor. Comput. Sci.*, vol. 392, pp. 5–22, 2008.

19. K. Cole-McLaughlin, H. Edelsbrunner, J. Harer, V. Natarajan, and V. Pascucci, "Loops in reeb graphs of 2-manifolds," in *Proc. of the 19th SoCG*, SCG '03, (New York, NY, USA), pp. 344–350, ACM, 2003.

20. Y. Shinagawa, T. Kunii, and Y. Kergosien, "Surface coding based on morse theory," *IEEE Comput. Graph. Appl.*, vol. 11, pp. 66 –78, sep 1991.

21. Y. Shinagawa and T. Kunii, "Constructing a reeb graph automatically from cross sections," *IEEE CG&A*, vol. 11, pp. 44 –51, nov 1991.

22. F. Lazarus and A. Verroust, "Level set diagrams of polyhedral objects," in *In Proc. of the 5th Symposium on Solid Modeling*, pp. 130–140, ACM, 1999.

23. J. Tierny, J. Vandeborre, and M. Daoudi, "3d mesh skeleton extraction using topological and geometrical analyses," in *In Proc. of the 14th Pacific Graphics 2006*, (Taipei, Taiwan), pp. 85–94, 2006.

24. V. Pascucci, G. Scorzelli, P.-T. Bremer, and A. Mascarenhas, "Robust on-line computation of reeb graphs: simplicity and speed," *ACM Trans. Graph.*, vol. 26, July 2007.

25. H. Doraiswamy and V. Natarajan, "Efficient algorithms for computing reeb graphs," *Comp. Geom.*, vol. 42, no. 6-7, pp. 606–616, 2009.

26. S. Berretti, A. Del Bimbo, and P. Pala, "3d mesh decomposition using reeb graphs," *Image Vision Comput.*, vol. 27, no. 10, pp. 1540 – 1554, 2009. Special Section: Computer Vision Methods for Ambient Intelligence.

27. G. Patane, M. Spagnuolo, and B. Falcidieno, "A minimal contouring approach to the computation of the reeb graph," *IEEE TVCG*, vol. 15, pp. 583–595, 2009.

28. L. Brandolini and M. Piastra, "Computing the reeb graph for triangle meshes with active contours," in *In Proc. of ICPRAM 2012, Volume 2*, pp. 80–89, SciTePress, 2012.

29. B. Fischl, D. Salat, E. Busa, M. Albert, M. Dieterich, C. Haselgrove, A. van der Kouwe, R. Killiany, D. Kennedy, S. Klaveness, A. Montillo, N. Makris, B. Rosen, and A. Dale, "Whole brain segmentation: automated labeling of neuroanatomical structures in the human brain," *Neuron.*, vol. 33, pp. 341–355, 2002.

30. A. Hamza and H. Krim, "Geodesic object representation and recognition," in *In Proc. of DGCI*, pp. 378 – 387, 2003.

31. X. Ni, M. Garland, and J. Hart, "Fair morse functions for extracting the topological structure of a surface mesh," *ACM Trans. Graph.*, vol. 23, pp. 613–622, Aug. 2004.

32. M. Novotni and R. Klein, "Computing geodesic distances on triangular meshes," in *In Proc. of WSCG-2002*, pp. 341–347, 2002.

33. E. Dijkstra, "A note on two problems in connexion with graphs," *Numer. Math.*, vol. 1, pp. 269–271, 1959.

34. M. Laakso, J. Tiihonen, E. Syvälahti, H. Vilkman, A. Laakso, B. Alakare, V. Räkköläinen, R. Salokangas, E. Koivisto, and J. Hietala, "A morphometric mri study of the hippocampus in first-episode, neuroleptic-naïve schizophrenia," *Schizophr. Res.*, vol. 50, no. 1 - 2, pp. 3 – 7, 2001.

35. J. Lötjönen, P.-J. Reissman, I. Magnin, and T.Katila, "Model extraction from magnetic resonance volume data using the deformable pyramid," *Med. Image Anal.*, vol. 3, no. 4, pp. 387 – 406, 1999.

36. D. G. Kendall, "A survey of the statistical theory of shape," *Statist. Sci.*, vol. 4, no. 2, pp. 87– 99, 1989.

37. K. Arun, T. Huang, and S. Blostein, "Least-squares fitting of two 3-d point sets," *IEEE Trans. Pattern. Ana.l Mach. Intell.*, vol. 9, no. 5, pp. 698–700, 1987.

38. D. Huttenlocher, G. Klanderman, and W. Rucklidge, "Comparing images using the hausdorff distance," *IEEE Trans. Pattern Anal. Mach. Intell.*, vol. 15, pp. 850 – 863, sep 1993.

39. K. Arun, T. Huang, and S. Blostein, "Closed-form solution of absolute orientation using unit quaternions," *J. Opt. Soc. Am. A.*, vol. 4, no. 4, pp. 629 – 642, 1987.